

# MODELING THE X-RAYS FROM THE CENTRAL COMPACT OBJECT PSR J1852+0040 IN KESTEVEN 79: EVIDENCE FOR A STRONGLY MAGNETIZED NEUTRON STAR

SLAVKO BOGDANOV

Columbia Astrophysics Laboratory, Columbia University, 550 West 120th Street, New York, NY 10027, USA  
 slavko@astro.columbia.edu

*Accepted for publication to the Astrophysical Journal on June 2, 2014*

## ABSTRACT

I present modeling of the X-ray pulsations from the central compact object (CCO) PSR J1852+0040 in the Galactic supernova remnant Kesteven 79. In the context of thermal surface radiation from a rotating neutron star, a conventional polar cap model can reproduce the broad, large-amplitude X-ray pulse only with a “pencil plus fan” beam emission pattern, which is characteristic of strongly magnetized ( $\gtrsim 10^{12}$  Gauss) neutron star atmospheres, substantially stronger than the  $\sim 10^{10}$  Gauss external dipole field inferred from the pulsar spin-down rate. This discrepancy can be explained by an axially displaced dipole. For other beaming patterns, it is necessary to invoke high-aspect-ratio emitting regions that are greatly longitudinally elongated, possibly due to an extremely offset dipole. For all assumed emission models, the existence of strong internal magnetic fields ( $\gtrsim 10^{14}$  Gauss) that preferentially channel internal heat to only a portion of the exterior is required to account for the implied high-temperature contrast across the stellar surface. This lends further observational evidence in support of the “hidden” strong magnetic field scenario, in which CCOs possess strong submerged magnetic fields that are substantially stronger than the external dipole field, presumably due to burial by fallback of supernova ejecta. I also conduct phase-resolved X-ray spectroscopy and find no evidence for prominent spin-phase-dependent absorption features that could be produced by cyclotron absorption/scattering.

*Subject headings:* pulsars: general — pulsars: individual (PSR J1852+0040, PSR J0821–4300) — stars: neutron — X-rays: stars

## 1. INTRODUCTION

Central compact objects (CCOs) constitute a group of X-ray-emitting, radio-quiet neutron stars found near the centers of supernova remnants (SNRs). To date, X-ray pulsations have been firmly detected from only three CCOs. They have relatively long spin periods (0.1 – 0.4 s), and long-term monitoring shows that their period derivatives ( $\dot{P} \equiv dP/dt$ ) are remarkably small, suggesting weak surface magnetic fields<sup>1</sup>. See Halpern & Gotthelf (2010), Gotthelf & Halpern (2009); Gotthelf et al. (2013), and Ho (2013) for observations and overview of related theory. Due to the limited sample of CCOs that exhibit X-ray pulsations, the physical mechanism responsible for their X-ray emission is not well understood, and their active lifetime and long-term evolution are poorly constrained. It remains unclear if CCOs are active radio pulsars beamed away from us or if the radio emission mechanism is intrinsically inoperative. Since CCOs are associated with very young SNRs, their nature and evolution are highly relevant to the neutron star production rate and the physics underlying the diversity of neutron stars produced by core collapse.

The compact X-ray source CXOU J185238.6+004020 was discovered in the center of the SNR Kesteven 79 by Seward et al. (2002). Subsequently, Gotthelf et al. (2005) discovered 105 ms pulsations from this CCO, now named PSR J1852+0040, establishing it as a young neutron star. A dedicated long-term X-ray timing cam-

paign of PSR J1852+0040 facilitated the first definite measurement of the spin-down rate of a CCO pulsar by Halpern & Gotthelf (2010). The measurements of  $P = 0.105$  s and  $\dot{P} = 8.7 \times 10^{-18}$  s s<sup>-1</sup>, imply in the dipole spin-down formalism a surface magnetic field strength of only  $B_{\text{surf}} = 3.1 \times 10^{10}$  G; on this basis, it has been termed an “anti-magnetar”. With a bolometric luminosity of  $3.0 \times 10^{33}$  erg s<sup>-1</sup>, an order of magnitude higher than its spin-down power  $\dot{E} \propto \dot{P}P^{-3} = 3.0 \times 10^{32}$  erg s<sup>-1</sup>, the X-ray radiation from PSR J1852+0040 is clearly not powered by the rotational kinetic energy of the star, thus requiring an additional energy source, such as residual cooling or low-level accretion.

The thermal X-ray emission from PSR J1852+0040 is characterized by a single unusually broad pulse, with a very high pulsed fraction of  $64\% \pm 2\%$ . X-ray observations spanning nearly five years are consistent with steady flux. Fitting of the X-ray spectrum to two blackbodies finds small emitting radii ( $R_1 = 1.9$  km and  $R_2 = 0.45$  km, for components of  $kT_1 = 0.30$  keV and  $kT_2 = 0.52$  keV, respectively; Halpern & Gotthelf 2010). Such small, hot regions are common among CCOs and are at odds with the inferred magnetic field strength since highly non-uniform surface temperature is usually attributed to the effects of much stronger magnetic fields. Thus it is unclear whether CCOs are intrinsically weakly magnetized neutron stars or whether they possess substantially stronger internal magnetic fields than the measured  $\sim 10^{10}$  G surface dipole field. This fundamental question regarding the nature of CCOs has generated a flurry of theoretical efforts aimed at constraining the key physics

<sup>1</sup> By assuming dipole spin-down, the surface field strength can be inferred from  $B_{\text{surf}} \equiv 3.2 \times 10^{19} (P\dot{P})^{1/2}$  G, where  $P$  is in seconds.

TABLE 1  
*XMM-Newton* X-RAY TIMING OBSERVATIONS OF PSR  
 J1852+0040.

ObsID	Date (UT)	Exposure <sup>a</sup> (ks)
0204970201	2004 Oct 18	30.6
0204970301	2004 Oct 23	30.5
0400390201	2006 Oct 08	29.7
0400390301	2007 Mar 20	30.5
0550670201	2008 Sep 19	21.2
0550670301	2008 Sep 21	31.0
0550670401	2008 Sep 23	34.8
0550670501	2008 Sep 29	33.0
0550670601	2008 Oct 10	36.0
0550671001	2009 Mar 16	27.0
0550670901	2009 Mar 17	26.0
0550671201	2009 Mar 23	27.3
0550671101	2009 Mar 25	19.9
0550671301	2009 Apr 04	26.0
0550671901	2009 Apr 10	30.5
0550671801	2009 Apr 22	28.0

<sup>a</sup> Total observing time not corrected for the 29% dead time of the EPIC pn small window mode.

and evolutionary fate of these enigmatic objects (see, e.g., Ho 2011; Shabaltas & Lai 2012; Viganò & Pons 2012; Bernal et al. 2013; Perna et al. 2013). It is highly likely that the heat distribution on the stellar surface closely traces the magnetic field structure. Therefore, constraining the surface emission properties and heat distribution of PSR J1852+0040 can help resolve this essential mystery of CCOs.

In this paper, I present modeling of the pulsed thermal X-ray emission from PSR J1852+0040 aimed at constraining key aspects of CCO physics based on the extensive set of archival *XMM-Newton* observations. The work is organized as follows. In §2 I summarize the archival data set and the data reduction procedures. In §3 I describe the numerical model employed in this study, while in §4 I show the results of the modeling. In §5 I present a pulse-phase-resolved spectroscopic analysis. I discuss the implications of the results in §5 and offer conclusions in §6.

## 2. DATA REDUCTION

I have retrieved the set of 16 archival *XMM-Newton* European Photon Imaging Camera (EPIC) pn (Strüder et al. 2001) observations of PSR J1852+0040, for a combined 327 kiloseconds of net exposure time (see Table 1). All exposures were obtained in small window mode, which affords a 5.7 ms time resolution but at a cost of 29% dead time during which no X-ray events are recorded. Each ODF data set was reprocessed with the SAS<sup>2</sup> version `xmmsas.20120523.1702-12.0.0` `epchain` pipeline to ensure that the latest calibration products and clock corrections (including leap seconds) are applied. The data were then filtered using the recommended standard pattern, flag, and pulse invariant values. None of the observations exhibit instances of high background flares.

For the purposes of the analyses presented below, the photon arrival times from each observation were

<sup>2</sup> The *XMM-Newton* SAS is developed and maintained by the Science Operations Centre at the European Space Astronomy Centre and the Survey Science Centre at the University of Leicester.

translated to the solar system barycenter with the SAS `barycen` tool assuming the DE405 solar system ephemeris. The corrected arrival times were folded coherently at the pulsar period using the ephemeris presented in Halpern & Gotthelf (2010). Relative to this previous analysis, which was based on the same data set but processed with SAS version `xmmsas.20060628.1801-7.0.0`, there is a systematic offset of +2.9 ms in all photon arrival times. This difference can be attributed to improvements in the *XMM-Newton* clock corrections. For all practical purposes this discrepancy is negligible and does not affect the results and conclusions of Halpern & Gotthelf (2010).

The X-ray events from the pulsar was extracted from a 12'' radius circle. This relatively small region was chosen so as to minimize the contribution of the diffuse emission from the supernova remnant. An important prerequisite for the pulse profile analysis described below is a reliable estimate of the background level at the source position. However, due to the relatively bright diffuse emission, coupled with the complicated morphology of the portion of the remnant that falls within the small-window mode *XMM-Newton* images, there is no obvious choice for a background extraction region. For this purpose, I take advantage of the sub-arcsecond resolution of the archival 30 ks *Chandra* ACIS-S image of Kes 79 (ObsID 1982) to identify a representative background region. I estimated the background level at the pulsar position by extracting counts from an annulus with inner radius of 2'', beyond which the point source emission becomes negligible, and outer radius of 12''. The resulting value was used to identify a larger background region with a matching surface brightness (i.e., count rate per unit area).

## 3. THE NUMERICAL MODEL

### 3.1. System Geometry and General Relativity

To study the pulsed X-rays from PSR J1852+0040, I employ a numerical model of surface emission from a neutron star assuming a Schwarzschild metric to describe the properties of the space-time in the vicinity of the star. It follows the basic formalism first presented by Pechenick et al. (1983) and used in a host of subsequent works (e.g., Ftaclas et al. 1986; Riffert & Mészáros 1988; Miller & Lamb 1998; Cropper et al. 2001; Weinberg et al. 2001; Beloborodov 2002; Poutanen & Gierliński 2003; Viironen & Poutanen 2004; Gotthelf et al. 2010). I represent the thermally-emitting pulsar by a neutron star of mass  $M$ , radius  $R_{NS}$ , spin period  $P$ , with different arrangements of X-ray-emitting surface elements on an otherwise cold neutron star. The surface normal of each element is at a position angle  $\alpha$  relative to the spin axis, while the line of sight to the observer is at an angle  $\zeta$  relative to the spin axis. The location of an X-ray-emitting surface element on a neutron star relative to the observer as a function of the time-varying rotational phase of the pulsar,  $\phi(t)$ , is then defined by the angle  $\theta$  between the normal to the surface and the line of sight:

$$\cos \theta(t) = \sin \alpha \sin \zeta \cos \phi(t) + \cos \alpha \cos \zeta \quad (1)$$

As the pulsar rotates, the varying projection of the emission area(s) causes flux variations (i.e. pulsations), with shape and amplitude determined in great part by the

combination of  $\alpha$  and  $\zeta$ . Note that by convention  $\alpha$  is reckoned from the spin pole towards the equator. The observed flux per unit energy from an emitting region is given by

$$F(E) = I(E)d\Omega \quad (2)$$

where  $I(E)$  is the intensity of the radiation as measured by a distant observer and  $d\Omega$  is the apparent solid angle subtended by the emission region. Transforming both quantities to the rest frame of the emitting region yields

$$F(E) = (1 - R_S/R_{NS})^{1/2} I'(E', \theta') \cos \theta \frac{d \cos \theta}{d \cos \psi} \frac{dS'}{D^2} \quad (3)$$

where the primed quantities are measured in the NS surface rest frame (Poutanen & Gierliński 2003), with  $dS \cos \theta = dS' \cos \theta'$ .  $R_S \equiv 2GM/c^2$  is the Schwarzschild radius,  $I'(E', \theta')$  is the emergent intensity, which may be a function of emission angle in addition to energy,  $dS'$  is the emission area and  $D$  is the distance.

A photon emitted at an angle  $\theta > 0$  with respect to the local radial direction follows a curved trajectory and is observed at infinity at an angle  $\psi > \theta$ . The relation between these two angles is given by (Pechenick et al. 1983):

$$\psi = \int_R^\infty \frac{dr}{r^2} \left[ \frac{1}{b^2} - \frac{1}{r^2} \left( 1 - \frac{R_S}{r} \right) \right]^{-1/2} \quad (4)$$

where

$$b = \frac{R_{NS}}{\sqrt{1 - R_S/R_{NS}}} \sin \theta \quad (5)$$

is the impact parameter at infinity of a photon emitted from radius  $R_{NS}$  at an angle  $\theta$ . For most real-world applications, including the analysis presented herein, a simplified approximate relation between  $\psi$  and  $\theta$  (Beloborodov 2002) can be used:

$$\cos \psi \approx \frac{\cos \theta - R_S/R_{NS}}{1 - R_S/R_{NS}} \quad (6)$$

which is valid for  $R_{NS} > 2R_S$ . This approximation greatly boosts the computational speed of the model while still maintaining a high degree of accuracy ( $\lesssim 3\%$  error for  $R \geq 3R_S$ ), allowing a thorough exploration of the model phase space and implementation of more complex emission regions. Owing to the relatively long spin period, special relativistic effects, such as Doppler boosting and aberration, as well as travel time differences are completely negligible (Poutanen & Gierliński 2003).

The total observed flux for a given rotational phase is found by relating  $\phi$  and  $\theta$  for a given emitting region through  $\psi$  via equations (1) and (4), using the desired  $I'(E', \theta')$  in equation (3), and summing the computed flux from all surface elements. This approach can be used to construct an arbitrary emission region on the NS surface by considering any number and arrangement of surface elements, provided they are sufficiently point-like so as not to introduce significant errors in the model (see, e.g., Turolla & Nobili 2013).

### 3.2. Surface Emission Model

The surface composition of PSR J1852+0040, and CCOs in general, is highly uncertain as there are multiple plausible possibilities. For instance, a light element

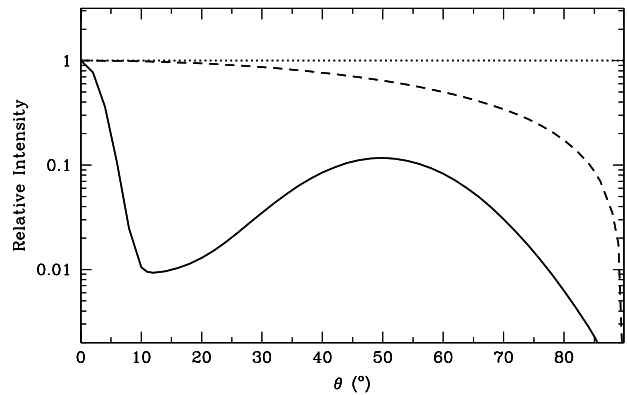


FIG. 1.— The relative intensities as a function of angle with respect to the surface normal ( $\theta$ ) for the three emission patterns considered in this analysis: isotropic (dotted), cosine beaming (dashed), and “pencil plus fan” beaming (solid).

atmosphere may, in principle, build up due to spallation of fallback material after the supernova explosion. Due to gravitational sedimentation, as the lightest elements, hydrogen or helium are expected to surface rapidly and thus dominate the surface emission if a layer thicker than  $\sim 1$  cm accumulates (Chang & Bildsten 2004). On the other hand, if no accretion takes place or if thermonuclear reactions occur after accretion, a mid-Z element (see, e.g., Mori & Ho 2007; Ho & Heinke 2009; Chang et al. 2010) or iron atmosphere may be present. The same is likely to be the case if any pulsar wind outflow is active that prevents accretion of material from the remnant. It is also quite possible that the stellar surface is devoid of an atmospheric layer, in which case the emission from the condensed neutron star surface may be reasonably well approximated by a blackbody (Potekhin et al. 2012).

Although based on the spin-down measurement the implied surface field at the magnetic equator of PSR J1852+0040 is  $3.1 \times 10^{10}$  G, the strong X-ray pulsations may be a manifestation of a substantially stronger field at the location of the hot regions, although the value cannot be easily determined as there are no obvious absorption features (see §5.1). This poses an additional difficulty in choosing the appropriate surface radiation model, considering that the emission characteristics of neutron star atmospheres can differ markedly between  $\sim 10^{10}$  G (Suleimanov et al. 2012),  $\sim 10^{12}$  G (Pavlov et al. 1994; Zavlin et al. 1995), and  $\gtrsim 10^{14}$  G (e.g., van Adelsberg & Lai 2006). As a consequence, any inferences drawn from modeling the thermal emission are likely to be dependent on the true surface magnetic field strength and its orientation relative to the surface.

For strongly magnetized atmospheres ( $\gtrsim 10^{12}$  G), a narrow “pencil” beam along the direction of the magnetic field can also appear in instances when the observers line of sight crosses the magnetic field lines, as well as a broad “fan” beam with peak intensity at intermediate angles with respect to the surface normal (see, e.g., Pavlov et al. 1994; Zavlin et al. 1995). For weakly magnetic models ( $\lesssim 10^{10}$  G), the emergent intensity declines with increasing angle with respect to the surface normal, resulting in a limb-darkening effect (Romani 1987; Zavlin et al. 1996). For atmospheres with  $\sim 10^{10-11}$  G, the emission is strongly beamed at photon energies coin-

cident with the harmonics of the cyclotron resonance frequency, with the strongest beaming occurring at the fundamental frequency and becoming progressively weaker with increasing harmonic number. Away from the cyclotron absorption lines, the emission generally declines with increasing angle away from the surface normal (see Suleimanov et al. 2010, in particular their Figure 7).

Based on this information, to account for the variety of possible angle-dependent intensity patterns of the thermal radiation from PSR J1852+0040, I consider three possibilities: (i) a standard isotropically emitting Planck spectrum; (ii) an emission model with a cosine dependence of the intensity as a function of emission angle relative to the surface normal as a proxy for a weakly magnetic neutron star atmosphere, including a  $\sim 10^{10}$  G light-element atmosphere at photon energies away from the cyclotron harmonics<sup>3</sup>; and (iii) a “pencil plus fan” beam pattern characteristic of strongly magnetic atmospheres for the case of a magnetic field perpendicular to the surface<sup>4</sup>. The three emission patterns are illustrated in Figure 1. Although none of the models account for the energy-dependence of the emergent intensity patterns of realistic atmosphere models (Romani 1987; Shibano et al. 1992; Pavlov et al. 1994; Zavlin et al. 1995), for the purposes of this analysis the latter two provide an adequate representation of the angular dependence (i.e. “beaming”) produced by a variety of neutron star atmospheres, while being substantially less computationally demanding than the full models. Therefore, although the exact values of the parameters derived throughout this analysis may not correspond to the actual values, the general conclusions regarding the emission properties and heat distribution of the stellar surface should be robust.

Neutron star atmospheres have the general property of producing continuum radiation with peak intensities at higher energies relative to a Planck spectrum for the same effective temperature (Romani 1987; Shibano et al. 1992; Ho & Lai 2001). As a consequence, when applied to thermal spectra they tend to yield lower temperatures and hence larger inferred emitting areas compared to a blackbody model. To account for this property while minimizing the additional computational cost, for the cosine beaming model, I use the empirical relation for non-magnetic H atmospheres given by McClintock et al. (2004; see in particular their equations A17 and A18). For the pencil plus fan beam model, I implement a “color correction”, obtained as follows. The spectrum of PSR J1852+0040 was fitted separately with a blackbody model and a magnetic *nsa* atmosphere with  $1 \times 10^{12}$  G. The ratio of the derived emitting areas from the two models as a function of temperature was used as a multiplicative factor to correct the flux normalization in the pulse profile fits in order to obtain emitting areas comparable to those of an actual magnetic atmosphere model.

### 3.3. Emission Region Geometry

<sup>3</sup> As shown in §5, the phase-resolved spectra of PSR J1852+0040 exhibit no strong cyclotron harmonics so this assumption is appropriate.

<sup>4</sup> As an approximation, I adopt the H atmosphere beaming pattern from Pavlov et al. (1994) for  $T_{\text{eff}} = 10^6$  K and  $B = 4.7 \times 10^{12}$  G at a photon energy of 2.28 keV.

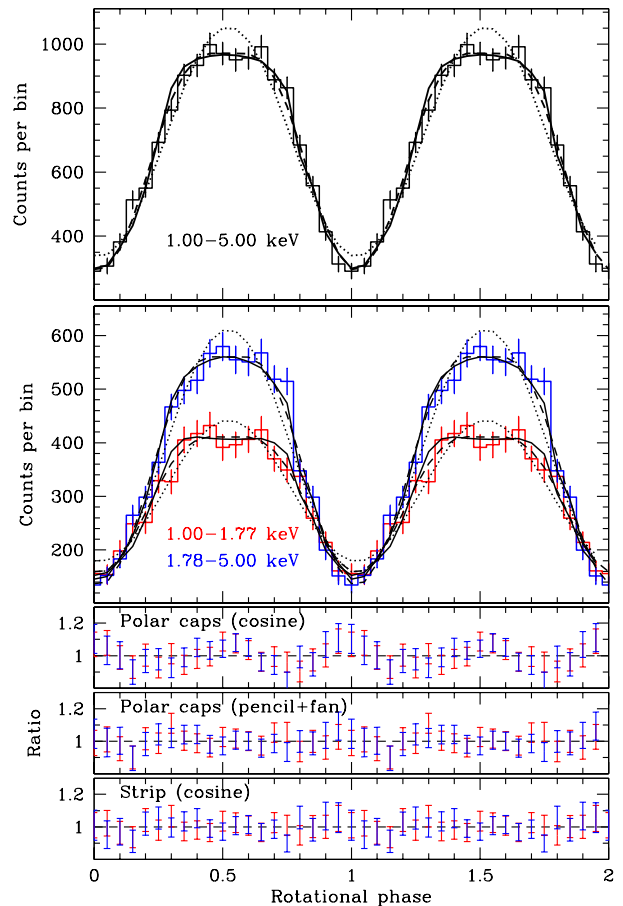


FIG. 2.— (Top) *XMM-Newton* EPIC pn background-subtracted pulse profile of PSR J1852+0040 in the 1–5 keV interval. (Middle) Pulse profiles in the 1–1.77 and 1.78–5 keV bands. The solid lines show the best fit for a rotating neutron star with two circular, antipodal hot spots for a “pencil plus fan” beam pattern. The dashed lines represent the best fit models of a rotating NS with a longitudinally extended hot strip across the surface for a cosine beaming emission model. The dotted lines correspond to the best fit for a rotating neutron star with two circular, non-antipodal hot spots for a cosine beaming model. The cosine and isotropic models produce virtually identical pulse profiles and residuals for both cases so only the former is shown. In all cases, a neutron star with  $M = 1.4 M_{\odot}$  and  $R_{\text{NS}} = 12$  km is assumed. The bottom three panels show the best fit residuals for the circular polar cap and strip models. Two rotational cycles are shown for clarity.

The spectra and pulse profiles accumulated from PSR J1852+0040 imply one or more multi-temperature hot emission regions that are significantly smaller than the full neutron star surface. For pulsar in general, the location and geometry of the heated regions is determined by the magnetic field structure at or beneath the stellar surface (e.g., Heyl & Hernquist 1998, 2001; Potekhin & Yakovlev 2001; Geppert et al. 1999, 2006; Pérez-Azorín et al. 2006; Pons et al. 2009), meaning that the surface emission can serve as a valuable tracer of the field topology. Previous studies by Shabaltas & Lai (2012) and Perna et al. (2013) have attempted to reproduce the observed pulse properties of PSR J1852+0040 by computing the expected surface heat signature of various assumed magnetic field configurations. However, for the temperature distributions and emission models considered in these investigations, the broad pulse shape

and the large pulse amplitude could not be simultaneously accounted for, hinting at a strongly anisotropic emission pattern and/or a non-standard arrangement of magnetic fields. Herein, rather than start from an assumed magnetic field configuration, I adopt the converse approach and aim to deduce the surface emission properties and magnetic field topology based on the heat distributions that can reproduce the phenomenology of PSR J1852+0040 by fitting the synthetic pulse profiles directly to the X-ray data.

For many thermally-emitting pulsars, a pair of circular hot spots, presumably corresponding to the pulsar magnetic polar caps, provides an adequate description of the observed thermal X-ray pulse profile. Based on this, I consider antipodal as well as non-antipodal polar caps (arising, for instance, due to an offset dipole), following both the treatment of point-like hot spots presented in Beloborodov (2002) and of extended circular polar caps described in Gotthelf et al. (2010) and Turolla & Nobili (2013).

The unusual pulse morphology offers qualitative insight regarding the possible atmosphere emission pattern as well as the heat distribution on the stellar surface. In particular, the broad and effectively flat pulse peak requires that the flux from the star appear essentially unchanged to the observer for  $\sim 20$ – $30\%$  of the rotation period. This can be produced by either a strongly anisotropic emission pattern or a region on the surface that is elongated in the direction of rotation ( $\phi$ ). To explore the latter possibility, I focus on regions on the surface that are much more extended in longitude than in latitude. The simplest way to describe such a high aspect ratio region using  $\alpha$  and  $\phi$  is to consider a strip of emission at constant latitude, which can be parameterized by angular extents in longitude and latitude ( $\Delta\phi$  and  $\Delta\alpha$ , respectively), and the values of  $\alpha_o$  and  $\phi_o$  of the geometric center of the emitting region. For such a longitudinal strip, the area is obtained by computing the integral of the region on a sphere

$$\begin{aligned} A_{\text{strip}} &= R_{NS}^2 \int_{\phi_o - \Delta\phi}^{\phi_o + \Delta\phi} \int_{\alpha_o - \Delta\alpha}^{\alpha_o + \Delta\alpha} \sin \alpha \, d\alpha \, d\phi \\ &= 2R_{NS}^2 \Delta\phi_o [\cos(\alpha_o - \Delta\alpha) - \cos(\alpha_o + \Delta\alpha)] \quad (7) \end{aligned}$$

This heat distribution can be easily modeled using Equation 3 by dividing the emission region into a grid consisting of smaller surface elements, each with an area defined by Equation 7. Although as defined, the rectangular shape of the strips is obviously not natural, given the available photon statistics such a geometry is indistinguishable from a more plausible one, such as an elliptical region or a strip with rounded corners or semicircular end caps. Moreover, the computational speed afforded by this simple parametrization allows a thorough exploration of the model phase space to identify the general type of heat distributions that can reproduce the data.

#### 4. PULSE PROFILE MODELING RESULTS

To enable a direct comparison with observations, the synthetic pulse profiles generated using the model described above were first convolved with the EPIC pn detector response. As a consequence of the high hydrogen column density along the line of sight towards the

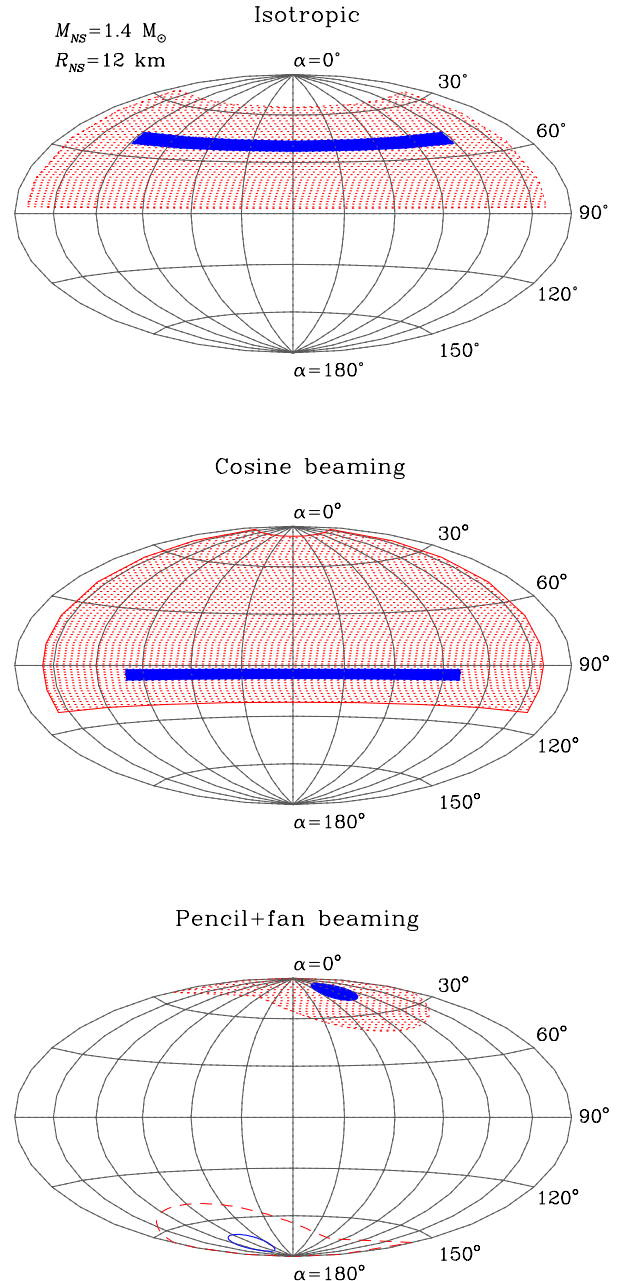


FIG. 3.— Hammer-Aitoff equal area projection of the surface of PSR J1852+0040 showing the likely temperature distribution inferred from the pulse profile modeling for an assumed neutron star radius of 12 km and mass  $1.4 M_{\odot}$ . The hot and warm regions are shown in blue and red, respectively. The isotropic, cosine, and pencil plus fan beam emission pattern results are shown from top to bottom, respectively. For the last case, the secondary polar cap does not contribute to the observed emission so only its outline is shown for reference.

pulsar, little useful spectral information is available below  $\sim 1$  keV. Based on this, I chose two energy bands which allows some sensitivity to the spectral shape of the radiation. The fits were performed simultaneously in two energy bands, 1.0–1.77 and 1.78–5.0 keV, in which the warm and hot thermal components dominate, respectively. Cooler surface emission from the rest of the neutron star is likely negligible above  $\sim 1$  keV so it is not



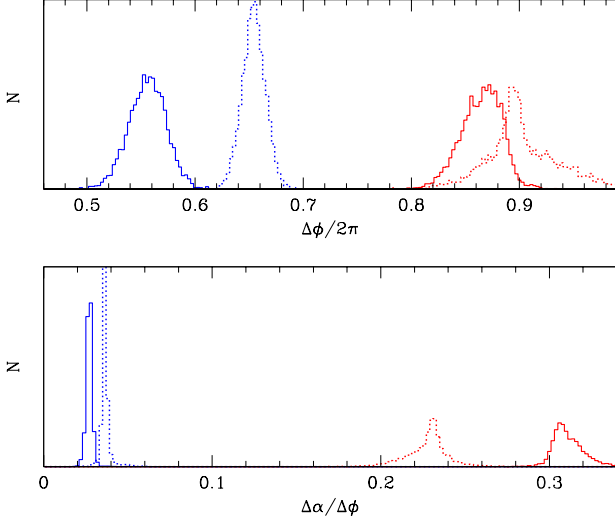


FIG. 4.— Summary of results of the pulse profile fits of PSR J1852+0040 derived from Monte Carlo simulations, assuming a neutron star with  $M = 1.4 M_{\odot}$  and  $R_{NS} = 12$  km. The solid lines and dotted lines correspond to the beamed and isotropic emission models, respectively. (Top) The fraction of the stellar circumference subtended by the hot (blue) and warm (red) emission regions in longitude at the latitude of the centroid of the strip,  $\Delta\phi/2\pi$  (Bottom) Aspect ratio ( $\Delta\alpha/\Delta\phi$ ) of the angular extent of the X-ray emitting regions in latitude ( $\Delta\alpha$ ) and longitude ( $\Delta\phi$ ).

modeled. Throughout the analysis, I assume a neutron star with  $M = 1.4 M_{\odot}$  and  $R_{NS} = 12$  km at a distance of  $D = 7.1$  kpc and  $N_H = 1.52 \times 10^{22} \text{ cm}^{-2}$  based on Giacani et al. (2009). To assess the dependence of the results on the highly uncertain neutron star compactness, the analysis was repeated for other values of  $R_{NS}$  in the range 9 – 15 km.

In the formal fits to the folded light curves I consider the allowed range of values for  $\alpha$  and  $\zeta$  ( $0^\circ - 180^\circ$ , and the range of acceptable emission region areas and temperatures as deduced from spectral fits. In the case of the circular cap model, I also consider the radius of each hot spot, while in the longitudinal strip model, the angular extents in longitude and latitude,  $\Delta\phi$  and  $\Delta\alpha$  are additional free parameters. Constraints on these parameters were derived via Monte Carlo simulations of  $5 \times 10^3$  realizations for each combination of stellar mass, radius and one of the three emission models described in §3.2. In the pulse profile fits, the emission regions were adaptively resized based on the input values of the angular extent of the entire region in each direction. The number of surface elements (90 and 45 in the  $\phi$  and  $\alpha$  directions, respectively) was chosen so as to ensure that the size of each is effectively point-like, which is the case for angular extents  $\lesssim 5^\circ$  (see Turolla & Nobili 2013). For both the polar cap and strip geometries, the hot and warm strips were allowed to intersect such that in the overlap region the emission is solely due to the hot region.

Figure 2 shows the best fits to the *XMM-Newton* EPIC pn pulse profile of PSR J1852+0040 with a model of a NS with a longitudinal heated strip, as well as a pair of circular, non-antipodal hot caps. For both the polar cap and strip geometries, the isotropic blackbody and cosine beaming models yield virtually identical best-fit model pulse profiles. For these emission patterns, it is apparent from the systematic residuals that the conven-

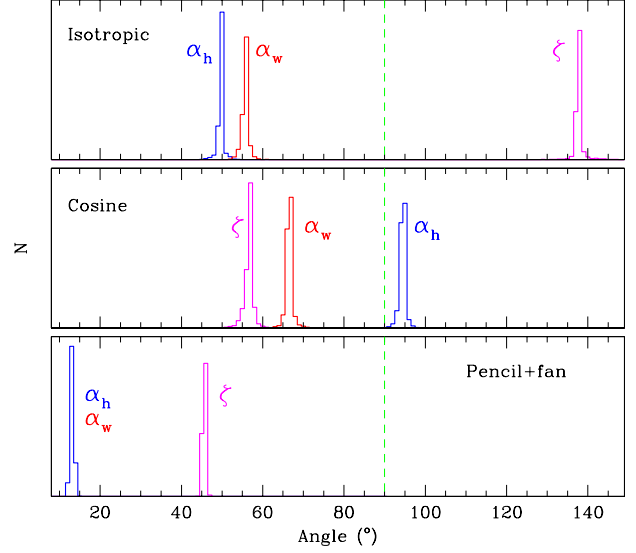


FIG. 5.— The constraints on the angle  $\alpha$  of the centroid of the hot (red) and warm (blue) regions and the viewing angle  $\zeta$  (magenta). The results for the isotropic, cosine, and pencil plus fan beam patterns are shown from top to bottom, respectively. For the latter, the hot and warm regions are co-located so  $\alpha$  is identical for both. In all cases, a symmetric set of model solutions is obtained if the three angles are mirrored about the stellar equator, corresponding to  $90^\circ$  in this plot (green dashed line).

tional polar cap model has difficulty simultaneously accounting for the wide and flattened peak and the narrow trough, even if the assumption of antipodal hot spots is relaxed. The best fit results in  $\chi_\nu = 1.48$  for 31 degrees of freedom. Therefore, if the surface emission exhibits an isotropic emission pattern or limb-darkening typical of weakly magnetized atmospheres, the heated regions on the surface of PSR J1852+0040 cannot be circular caps. In contrast, the “pencil plus fan” beam model can easily reproduce the pulse shape with the conventional antipodal polar cap model, yielding  $\chi_\nu = 0.90$  for 31 degrees of freedom. This is possible because of the fan component of the beam, which peaks at intermediate angles with respect to the surface normal (Figure 1) and is thus able to compensate for the decline in the projected area of the polar cap as the star rotates, resulting in a broad, flat-topped pulse. The best fit redshift-corrected temperatures are  $T_h = (7.4 \pm 0.6) \times 10^6$  K and  $T_w = (3.2 \pm 0.6) \times 10^6$  K, with the corresponding polar cap emission radii of  $R_h = 1.5 \pm 0.6$  km and  $R_w = 6.0 \pm 2.5$  km. The quoted uncertainties are at a  $1\sigma$  confidence level.

The elongated strip configuration is able to reproduce the pulse shape for both the isotropic and cosine beaming models, resulting in best fits with  $\chi_\nu = 0.95$  for 29 degrees of freedom in both instances. The isotropic emission model produces best fit temperatures (as measured at the neutron star surface) of  $T_h = (7.0 \pm 0.6) \times 10^6$  K and  $T_w = (3.3 \pm 0.8) \times 10^6$  K. The half-widths of the hot and warm regions in the latitudinal direction are  $R_{\alpha_h} = 0.7 \pm 0.3$  km  $R_{\alpha_w} = 6.5 \pm 1.4$  km, and  $R_{\phi_h} = 18.9 \pm 4.9$  km  $R_{\phi_w} = 28.2 \pm 7.1$  km in the longitudinal direction. For the cosine beaming model, the best fit parameters are  $T_h = (3.2 \pm 0.5) \times 10^6$  K and  $T_w = (1.7 \pm 0.6) \times 10^6$  K,  $R_{\alpha_h} = 0.56 \pm 0.11$  km and

$R_{\alpha_w} = 9.3 \pm 3.8$  km, and  $R_{\phi_h} = 20.9 \pm 6.3$  km and  $R_{\phi_w} = 24.2 \pm 8.4$  km. Note that for all three emission models, the quoted values of  $R_h$  and  $R_w$  correspond to arc lengths on the stellar surface.

For the assumed  $M = 1.4 M_\odot$ , the isotropic and cosine beaming emission pattern models produce no acceptable solutions for  $R_{NS} \lesssim 9$  km, while for the pencil plus fan beam, the same is true for  $R_{NS} \lesssim 8.5$  km. In the case of the isotropic model, this is expected since for more compact stars it is not possible to produce the remarkably large observed pulse amplitude because of the stronger gravitational bending of light effect, which acts to greatly diminish the amplitude of rotation-induced modulations (see, e.g., Psaltis et al. 2000). For beamed emission, this effect is not as strong and a much larger pulsed fractions can in principle be achieved for the same set of model parameters because the anisotropic emission pattern of the emergent intensity acts to counter the suppression of pulsations caused by light bending (see, e.g., Bogdanov & Grindlay 2009, for the case of the millisecond pulsar PSR J0030+0451, with a  $\sim 70\%$  thermal pulsed fraction). However, in the case of PSR J1852+0040 in particular, the area of the warm emission region required to produce a satisfactory fit exceeds the total surface area of a 9 km and 8.5 km neutron star, for the cosine and pencil plus fan beam patterns, respectively.

Figure 3 illustrates the most probable geometric configurations of the emission regions deduced from the pulse profile modeling for a neutron star with radius of 12 km. Similar configurations are obtained for the range of plausible neutron star radii considered in the analysis. Figures 4 and 5 show summary plots of the various parameters of the fit based on the array of Monte Carlo simulations. Several noteworthy features of the inferred emission regions are evident. In particular, for the isotropic and cosine beaming patterns, the results favor emission regions that have substantial elongation in the longitudinal direction, with aspect ratios ranging from 3:1 for the warm emission region to nearly 100:1 for the hot component. The requirement for such extreme aspect ratios to reproduce the data explains why the conventional polar cap model cannot fit the pulse profile using these emission patterns. Even in the case of two polar caps that are adjacent and aligned in the  $\phi$  direction, it is only possible to obtain an aspect ratio up to  $\sim 2:1$ .

As evident from Figure 3, for the elongated strip geometry the hot emission region tends to lie well away from the spin poles, which is a necessary condition for producing the large pulse amplitude at higher photon energies. The warm region is substantially more extended in both longitude and latitude, nearly wrapping around the star and covering up to  $\sim 50\%$  of the entire stellar surface (see, e.g., the top two maps in Figure 3). In general, the fits favor co-located hot and warm regions, especially a thin hot strip enveloped entirely by a much larger warm region. This suggest that the thermal X-ray radiation originates from a single contiguous multi-temperature region. It is possible that the strips are not at constant latitude, but are instead inclined with respect to the spin equator. However, accounting for this would require the introduction of an additional free parameter, which, given the excellent fit of the current model, is not warranted by the data. Moreover, any such inclination is likely small

(of order a few degrees) since a highly inclined hot strip would not reproduce the observed flat pulse.

The best fit for the pencil plus fan beam model places the polar caps near to the spin pole (which actually lies within the larger warm region; see bottom of Figure 3) but the highly anisotropic beaming pattern is still able to produce a large amplitude pulse. Although for the pencil plus fan beam model two identical, antipodal polar caps were assumed, for the best fit geometry, the second polar cap resides in the region not visible to the observer. As a result, identical results are obtained with a single polar cap and the properties of the second polar cap are poorly constrained.

For a given surface emission model and assumed stellar radius, the geometry and the location of the emission regions are very tightly constrained, owing to the unique morphology and large amplitude of the X-ray pulsations. It should be noted, however, if the possible values of the neutron star mass and radius, uncertain surface composition, and magnetic field strength are considered, the allowed range of the free parameters become quite large. In addition, although the X-ray emitting areas are assumed to be at two discrete temperatures, in reality, a smooth temperature gradient likely exists between the warm and hot regions.

## 5. PHASE-RESOLVED SPECTROSCOPY

### 5.1. A Search for Narrow Spectral Features

The available *XMM-Newton* data provide a sufficient harvest of source photons to allow an investigation of any phase-dependent spectral features. This is of particular relevance for CCOs given that 1E1207.4-5209 at the center of the supernova remnant PKS 1209-51/52 shows two distinct harmonically-related features at 0.7 and 1.4 keV (Bignami et al. 2003; De Luca et al. 2004), plus two features at 2.1 and 2.8 keV whose existence is questionable (Sanwal et al. 2002; Mori et al. 2005). These absorption exhibit remarkable variability as a function of spin phase. The most plausible interpretation is that they arise due to resonant cyclotron absorption, with the 0.7 keV feature corresponding to the fundamental frequency. If the absorption arises from electrons near the neutron star surface, the relation between the fundamental cyclotron energy (corrected for gravitational redshift) and magnetic field,  $E_c = \hbar e B / mc = 0.116 (B / 10^{10} \text{ G}) \text{ keV}$ , implies a field strength of  $8 \times 10^{10} \text{ G}$ . An alternative interpretation focuses on helium-like oxygen or neon in a magnetic field of  $\sim 10^{12} \text{ G}$  (see, e.g., Hailey & Mori 2002; Mori et al. 2005).

Motivated by this, I extracted phase-resolved spectra from the archival data in Table 1 using four equal pulse phase intervals:  $0.125 < \phi_1 < 0.375$ ,  $0.375 < \phi_2 < 0.625$ ,  $0.625 < \phi_3 < 0.875$ , and  $0.875 < \phi_4 < 1.125$ . As shown in Figure 2, as defined, phase zero coincides with the pulse minimum. For each spectrum, the counts were grouped so as to ensure at least 30 counts per energy bin. All four spectra were fitted jointly in XSPEC 12.7.1 (Arnaud 1996) with the same temperatures for all four phases but with independent flux normalizations.

In Halpern & Gotthelf (2010), only a blackbody and non-magnetic *nsa* models were considered. However, in the standard vacuum dipole radiation formalism the expected magnetic field strength at the magnetic poles of

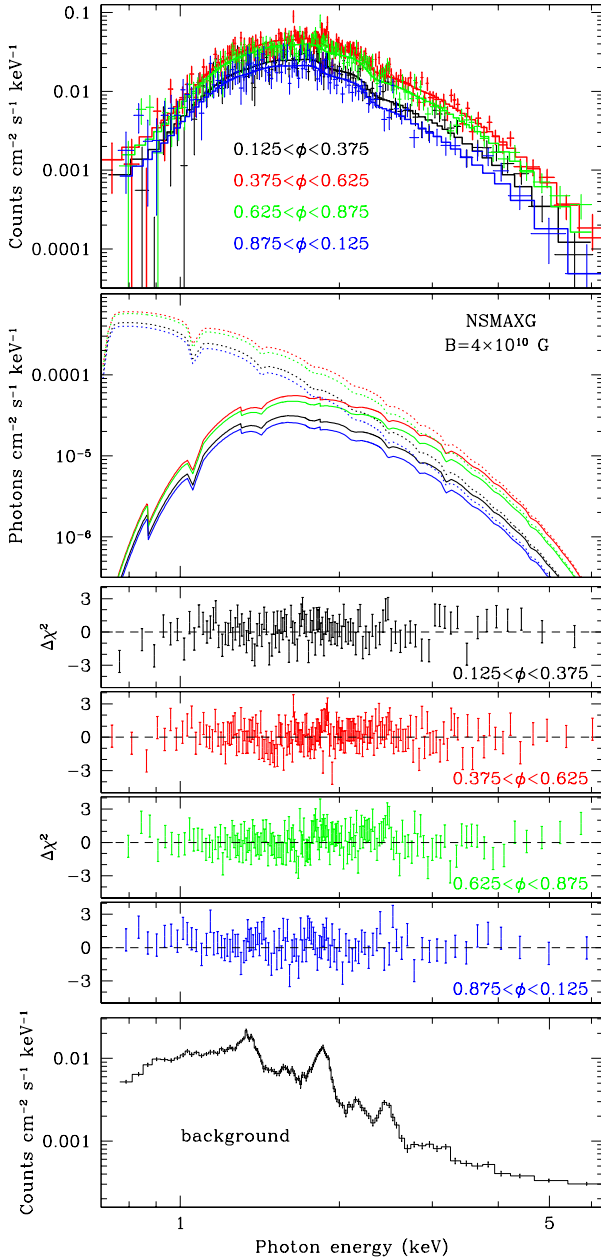


FIG. 6.— (Top) Pulse phase-resolved spectra of PSR J1852+0040 fitted with a two-temperature  $4 \times 10^{10}$  Gauss H atmosphere (*nsmaxg* model number 1060). The phase intervals are based on the pulse profiles in Figure 2. (Second from top) The best fit absorbed (solid) and unabsorbed (dotted) model spectrum. The four panels show the best fit residuals expressed in terms of  $\sigma$  with error bars of size one. (Bottom) The background spectrum used in the spectroscopic analysis.

PSR J1852+0040 is approximately  $2B_{\text{surf}} \simeq 6.1 \times 10^{10}$  G. A more realistic treatment (see, e.g., Spitkovsky 2006) yields  $(4 - 5) \times 10^{10}$  G, depending on the magnetic inclination. Based on this, I consider a model that is more appropriate for this pulsar – a two-temperature (*nsmaxg*) neutron star hydrogen atmosphere model with  $B = 4 \times 10^{10}$  G (Ho et al. 2008). Since the results from §4 for the pencil plus fan beam model suggest a substantially stronger field at the polar cap, I also employ the

*nsa* model with  $B = 1 \times 10^{12}$  G (Pavlov et al. 1994). In both cases, the models have been computed for  $M = 1.4 M_{\odot}$  and  $R_{\text{NS}} = 10$  km.

Statistically acceptable, equally good fits are obtained for both models (see Table 2). As evident from Figure 6, which shows the best *nsmaxg* model fit, several narrow-band residuals are apparent. However, the energies of these features coincide with features seen in the background spectrum (bottom panel of Figure 6). Based on this, I conclude that they arise due to imperfect background subtraction. As noted previously, PSR J1852+0040 is situated in a relatively X-ray-bright supernova remnant with significant spatially-dependent variations in brightness and spectral shape, causing difficulty in obtaining a representative background.

Aside from these features, no statistically significant phase-dependent residuals that could be plausibly associated with cyclotron absorption/scattering are seen in the spectrum of PSR J1852+0040. This is not surprising given that the weaker magnetic field derived from spin-down relative to 1E1207.4–5209 only produces weak features above  $\sim 1$  keV from the higher order cyclotron harmonics, as evident from the second panel from the top in Figure 6 (see also Suleimanov et al. 2010). The most prominent absorption features of the  $B = 4 \times 10^{10}$  G model, corresponding to the fundamental (at  $\sim 0.35$  keV) and first overtone ( $\sim 0.7$  keV) of the cyclotron resonance, would be severely attenuated by interstellar absorption, while the remaining features are too shallow to be identified in the present data given the limited energy resolution and insufficient photon statistics. In the  $\sim 10^{12}$  G scenario, no narrow-band spectral features are expected in the energy range under consideration.

The absence of any phase-dependent absorption features intrinsic to the pulsar in the spectrum indicates that the observed rotation-induced flux variations are unlikely to be due to phase-dependent resonant cyclotron scattering of the surface thermal X-rays from a uniformly emitting neutron star, as recently proposed for ordinary pulsars (see, e.g., Kargaltsev et al. 2012). Even in the case of 1E1207.4–5209, which unambiguously shows absorption features, the underlying cause for the pulsations is likely the changing view of the hot regions on the star due to rotation, with the resonant scattering only enhancing the rotation-induced flux modulations rather than being the sole cause.

## 5.2. A Carbon Atmosphere?

For the CCO in Cas A, the derived effective radii of the emission region for H and He atmosphere models ( $4 - 6$  km) are much smaller than the expected NS radius. Based on this and the apparent lack of X-ray pulsations, Ho & Heinke (2009) have argued that Cas A needs to be covered by a non-magnetic C atmosphere in order to produce an emission size  $R = 15.6_{-2.7}^{+1.3}$  km, assuming  $M = 1.4 M_{\odot}$  and  $D = 3.4$  kpc, that is consistent with the theoretical prediction for the radii of NSs. More recently, Klochkov et al. (2013) have applied a C atmosphere to the X-ray spectra of the CCO in the HESS J1731–347/G353.6–0.7 remnant obtaining good fits for plausible values of the neutron star mass and radius as well.

In light of these results it is interesting to compare the



TABLE 2  
HYDROGEN ATMOSPHERE SPECTRAL FITS FOR PSR J1852+0040.

Parameter <sup>a</sup>	Value
<b>nsmaxg<sup>b</sup> (<math>B = 4 \times 10^{10}</math> G)</b>	
$N_H$ ( $10^{22}$ cm <sup>-2</sup> )	1.52
$T_{\text{eff},1}$ ( $10^6$ K)	$3.46^{+0.11}_{-0.07}$
$T_{\text{eff},2}$ ( $10^6$ K)	$1.48^{+0.48}_{-0.35}$
$R_{\text{eff}}$ (km) <sup>c</sup>	$3.2^{+3.3}_{-2.9}$
$R_{\text{eff}}$ (km) <sup>c</sup>	$4.9^{+9.4}_{-4.9}$
$\chi^2_{\nu}/\text{dof}$	1.05/530
<b>nsa<sup>b</sup> (<math>B = 1 \times 10^{12}</math> G)</b>	
$N_H$ ( $10^{22}$ cm <sup>-2</sup> )	1.52
$T_{\text{eff},1}$ ( $10^6$ K)	$8.27^{+0.29}_{-0.31}$
$T_{\text{eff},2}$ ( $10^6$ K)	$3.07^{+0.24}_{-0.25}$
$R_{\text{eff},1}$ (km) <sup>c</sup>	$0.34^{+0.13}_{-0.11}$
$R_{\text{eff},2}$ (km) <sup>c</sup>	$3.5^{+1.8}_{-1.4}$
$\chi^2_{\nu}/\text{dof}$	1.06/530

<sup>a</sup> Quoted uncertainties are at a  $1\sigma$  confidence level for one interesting parameter.

<sup>b</sup> A neutron star of mass  $1.4 M_{\odot}$  and radius 10 km is assumed for both models.

<sup>c</sup> Redshift-corrected effective emitting radius assuming  $D = 7.1$  kpc.

C atmosphere fits to the phase-resolved spectra of PSR J1852+0040. For this purpose, I have applied the recently published *carbatm* model (Klochkov et al. 2013; Suleimanov et al. 2014) to the four phase-resolved spectra described in §5.1. Table 3 summarizes the best fit parameters for fixed  $D = 7$  kpc and  $M = 1.4 M_{\odot}$  and three assumed stellar radii: 9, 12, and 14 km. It is apparent that for 9 and 12 km, the inferred area at pulse maximum exceeds the total surface area of the star. Even in the case of 14 km, the implied emission area is equivalent to  $\approx 95\%$  of the NS surface. However, although a single-temperature C atmosphere model produces a statistically acceptable fit with  $R_{\text{eff}} \approx R_{\text{NS}}$ , this finding cannot be reconciled with the strongly pulsed X-rays from PSR J1852+0040, which indicate emission from a much smaller portion of the stellar surface.

After an age of about 1000 yr, a NS should cool enough to allow a light element atmosphere to accumulate (Chang et al. 2010). Based on this, as Cas A is only  $\sim 330$  yr old (Fesen et al. 2006), a C atmosphere may in fact be present on its surface (see, however, Posselt et al. 2013). On the other hand, the ages of PSR J1852+0040 and the CCO in G353.6–0.7 have been estimated to be 5400–7500 yr (Sun et al. 2004) and  $\sim 27,000$  yr (Tian et al. 2008), respectively. Therefore, there is no reason to expect a C atmosphere to dominate the surface emission in these older CCOs. Combined with this theoretical argument, the incongruity of the C atmosphere result with the strong X-ray pulsations from PSR J1852+0040 suggests that caution should be exercised when applying such spectroscopic models to other CCOs as it could lead to specious conclusions. This is especially true in cases where no pulsations have been detected, meaning that no information regarding the actual surface heat distribution can be gained.

## 6. DISCUSSION

### 6.1. Comparison with Other CCOs

TABLE 3  
CARBON ATMOSPHERE SPECTRAL FITS FOR PSR J1852+0040.

Parameter <sup>b</sup>	$R_{\text{NS}}$ (km) <sup>a</sup>		
	9 km	12 km	14 km
$N_H$ ( $10^{22}$ cm <sup>-2</sup> )	$1.55 \pm 0.04$	$1.52 \pm 0.04$	$1.50 \pm 0.04$
$T_{\text{eff}}$ ( $10^6$ K)	$2.11 \pm 0.05$	$1.91 \pm 0.05$	$1.84 \pm 0.05$
$A_{\text{eff}}/A_{\text{NS}}^c$	$1.61^{+0.29}_{-0.24}$	$1.16^{+0.21}_{-0.18}$	$0.95^{+0.18}_{-0.15}$
$\chi^2_{\nu}/\text{dof}$	1.11/534	1.11/534	1.11/534

<sup>a</sup> A neutron star mass of  $1.4 M_{\odot}$  is assumed in all cases.

<sup>b</sup> Quoted uncertainties are at a  $1\sigma$  confidence level for one interesting parameter.

<sup>c</sup> Effective emitting area expressed as a fraction of the total NS surface area assuming  $D = 7.1$  kpc.

The pulse profile shape of PSR J1852+0040, especially the very broad pulse, differs substantially from other thermally-emitting neutron stars, including other CCOs like PSR 0821–4300 in Puppis A, 1E1207.4–5209 in PKS 1209–51/52, suggesting substantial differences in temperature distribution and/or viewing geometry.

Gotthelf et al. (2010) conducted detailed modeling of the X-ray pulsations and spectra of PSR J0821–4300, the CCO in the SNR Puppis A. The analysis demonstrated that a pair of thermal, diametrically opposite hot spots on the surface is able to fully account for the observed two-component thermal spectrum and energy-dependent pulse profile, including the remarkable  $180^\circ$  phase reversal at  $\approx 1.2$  keV. However, the phase reversal requires that the temperatures of the two emission spots differ by a factor of two and their areas by a factor of  $\sim 20$ . In contrast, the markedly non-sinusoidal pulse profile of PSR J1852+0040 exhibits no energy dependent phase shift. This could indicate that, unlike PSR J0821–4300, the emission regions of different temperatures are either co-located on the surface or their centroids are effectively at the same longitude. Alternatively, this may be the direct result of a surface heat map comparable to PSR J0821–4300 but with different combination of magnetic inclination and viewing angle. For PSR J1852+0040, in the best-fit antipodal hot spot model obtained with the pencil plus fan beam emission model (see bottom panel of Figure 3), the secondary polar cap does not contribute significantly to the observed emission, which when combined with the severe interstellar absorption of emission below  $\sim 1$  keV, would not produce a pulse phase reversal due to a much larger, cooler antipodal cap.

The CCO 1E 1207.4–5209 exhibits much less pronounced X-ray pulsations, reaching a maximum  $\sim 14\%$  pulsed fraction in the fundamental cyclotron absorption feature at  $\sim 0.7$  keV (De Luca 2008). Aside from the enhancement in pulsations at energies coinciding with the absorption features, the low-amplitude and approximately sinusoidal pulsations suggest emission from a conventional hot-spot configuration. The evidence for a slight phase shift of the pulsations at energies below  $\sim 0.5$  keV, could be interpreted using the same heat distribution found for PSR J0821–4300 but with a different combination of  $\alpha$  and  $\zeta$ .

### 6.2. A Strongly Magnetized Hot Spot?

Shabaltas & Lai (2012) have attempted to account for the X-ray properties of PSR J1852+0040 by analyzing

the expected heat distribution and resulting X-ray light curves of a neutron star with a weak centered dipole plus a strong ( $\sim 10^{14}$  G) toroidal crustal magnetic field. The resulting heat distribution, characterized by small hot spots, is capable of achieving a high X-ray pulsed fraction (see Figures 2, 4, and 5 in Shabaltas & Lai 2012) but not a broad pulse shape that closely resembles that of PSR J1852+0040. A likely explanation for this is the assumption of a toroidal field that is large everywhere except near the magnetic polar caps. This results in a weak field ( $\sim 10^{10}$  G) at the polar caps, which (away from the lower order cyclotron harmonics) emits an emission pattern that is well-approximated by a cosine beaming function. As shown in §4, such an emission pattern cannot account for the observed pulsations for the standard antipodal hot spot model.

The spin-down measurement of PSR J1852+0040 implies a magnetic field at the magnetic poles of  $\sim 4 \times 10^{10}$  G (for  $R = 12$  km and moment of inertia  $I = 10^{45}$  g cm<sup>2</sup>). However, the excellent fits to the pulse profile with the polar cap model for the pencil plus fan beam emission model suggests that the magnetic field needs to be substantially higher ( $\gtrsim 10^{12}$  G) to produce such a highly anisotropic emission pattern. This is contradictory to the weak surface dipole field implied by the measured spin-down. One way to accommodate both findings is to displace the dipole field in the axial direction such that at the magnetic pole closer to the magnetic moment the field is significantly stronger, while at large distances from the stellar surface the field still appears weak ( $\sim 10^{10}$  G). In this sense, the implied heat distribution would be very similar to that inferred for PSR J0821–4300 in Puppis A (see Figure 7a). As noted in §6.1, in this case the markedly different pulse properties between the two CCOs can then be easily accounted for by different combinations of  $\alpha$  and  $\zeta$ .

### 6.3. An Extremely Offset Dipole?

The surface emission maps deduced using the isotropic and cosine beaming patterns are quite peculiar, as they imply a lack of discernable polar caps and the absence of azimuthal symmetry in the surface emission. This could, in principle, arise due to large deviations from a conventional centered magnetic field model. Perna et al. (2013) have investigated the surface temperature profiles for young, strongly magnetized ( $10^{13-15}$  G) neutron stars by considering both purely poloidal and a mixture of poloidal and toroidal components magnetic fields. Surprisingly, this analysis revealed that for  $\sim 5$  kyr-old neutron stars (comparable to the age of PSR J1852+0040) with both  $10^{14}$  G poloidal and  $5 \times 10^{15}$  G toroidal fields, the highest surface temperature is situated not at the magnetic poles but in circumferential bands at intermediate magnetic colatitudes, reminiscent of the strips illustrated in Figure 3. However, a key feature of the X-ray-emitting regions shown in Figure 3 is the azimuthal asymmetry, namely partial hot bands that do not completely encircle the star. Indeed, the inherently axisymmetric magnetic field configurations assumed in (Perna et al. 2013) and similar studies (e.g., Geppert et al. 2006) cannot simultaneously account for the broad pulse, narrow trough, and anomalously high pulsed fraction if blackbody or emission pat-

terns characteristic of weakly magnetized atmospheres are assumed. In principle, the necessary heat asymmetry can be achieved by displacing the magnetic moment from the center of the star or introducing a strong quadrupole component (provided that the associated sub-surface field is of sufficient strength to preferentially channel the interior heat to only a fraction of the surface; see §6.3). A large displacement (of order  $R_{NS}$ ) in a direction orthogonal to the dipole axis would cause the magnetic polar caps to become greatly elongated (as illustrated in Figure 7b). This strip may not in fact be contiguous, with a gap between the two “polar strips”, but at the phase resolution afforded by the photon statistics of the presently available data such a gap is not discernable.

### 6.4. Submerged Strong Magnetic Fields?

As noted by Halpern & Gotthelf (2010) and numerous subsequent works, the existence of hot areas that are a fraction of the total surface for CCOs is difficult to reconcile with an intrinsically weakly magnetized neutron star (i.e. an “anti-magnetar”) as it requires a mechanism to confine the heat to a small region. For strong fields, the heat conductivity is enhanced in the direction parallel to the magnetic field, while it is reduced in the perpendicular direction (e.g., Heyl & Hernquist 1998, 2001; Potekhin & Yakovlev 2001; Geppert et al. 1999, 2006; Pérez-Azorín et al. 2006; Pons et al. 2009). Hence, PSR J1852+0040 needs to possess a much larger “hidden” magnetic field in the crust than the dipole field inferred from the spin-down measurement from Halpern & Gotthelf (2010). This field acts as an insulator thus restricting the surface heat to a portion of the surface.

One plausible way to simultaneously account for the low apparent field as measured from spin-down and the strong sub-surface field required to explain the highly non-uniform surface heat distribution is to consider the fallback of the debris of the supernova explosion onto the newborn neutron star. In particular, shortly after the violent explosion, the neutron star is believed to accrete material from the reverse shock at a rate greatly exceeding the Eddington limit (e.g., Blondin 1986; Chevalier 1989; Houck & Chevalier 1991). This episode of so-called “hyper-critical” accretion could bury the magnetic field into the crust of the nascent neutron star, resulting in an apparent surface field substantially weaker relative to the internal “hidden” magnetic field (Viganò & Pons 2012; Bernal et al. 2013). A post-supernova accretion episode of  $10^{-4} - 10^{-3} M_{\odot}$  over a large region of the surface is necessary to bury the magnetic field into the inner crust. This burial process can, in principle, result in crustal magnetic fields with  $\sim 10^{14}$  G, which in turn, produce high temperature contrast across the stellar surface, while still maintaining a low apparent surface field.

The details of the current magnetic field topology presumably depend on the particular geometry of the supernova explosion ejecta, and may be the product of non-uniform fallback and/or low accretion rate (see Bernal et al. 2013). In this scenario, the peculiar heat distributions of PSRs J1852+0040 and J0821–4300 may be the direct result of the configuration of the fallback material. Alternatively, it is possible that the natal magnetic field of the neutron star deviated significantly from a centered dipole field in the first place, possibly

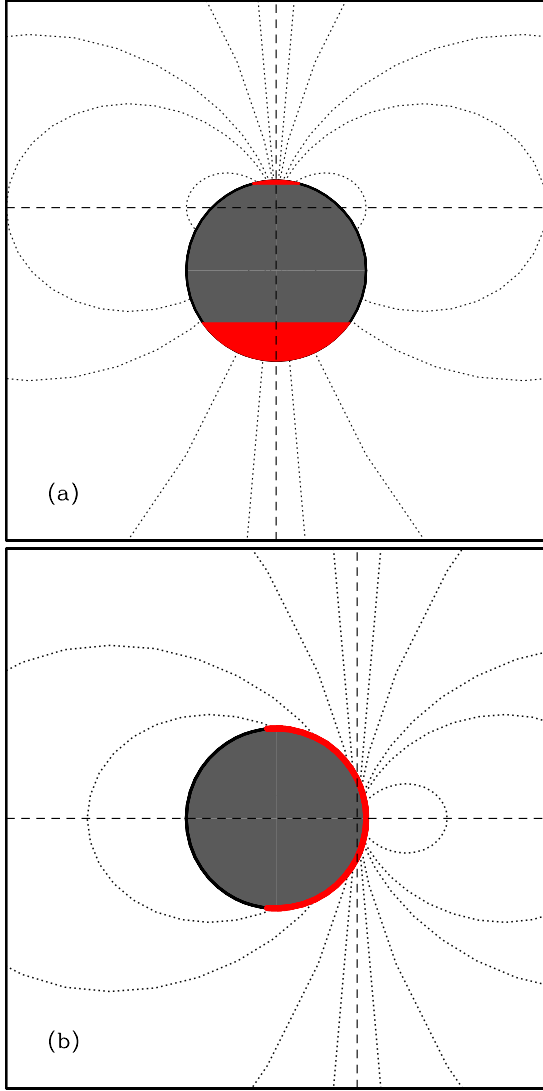


FIG. 7.— Schematic illustration of the possible offset magnetic dipole field configurations for PSRs J1852+0040 discussed in the text: (a) A dipole offset in the direction of the magnetic axis and (b) a dipole offset perpendicular to the magnetic axis. Scenario (a) is also applicable to PSR J0821–4300. The red shows the inferred X-ray emitting areas on the stellar surface. The dotted lines show the dipole magnetic field lines while the vertical and horizontal lines show the magnetic axis and equator, respectively.

due to an off-center explosion (Burrows & Hayes 1996; Lai & Goldreich 2000), and the fallback uniformly submerged the field while still preserving the initial global configuration but with a much weaker surface field.

An alternative interpretation for the restricted heat on the surface is on-going accretion of fall-back material at a sufficiently low rate via a thin disk. However, the steady spin-down over many years and the lack of evidence for any long-term X-ray variability do not favor this scenario. Localized heating due to a return current, driven by the rotation of the magnetized star, is also not likely as it requires rotation-power to supply the energy, but the observed X-ray luminosity greatly exceeds the spin-down luminosity of the pulsar.

## 7. CONCLUSION

I have presented modeling of the thermal X-ray pulsations from the central compact object and 105-millisecond X-ray pulsar PSR J1852+0040 in the Galactic supernova remnant Kesteven 79. Unlike previous studies (Shabaltas & Lai 2012; Perna et al. 2013), the relatively simple models employed herein are able to simultaneously account for both the X-ray pulse amplitude and broad peak. The unusual morphology of the pulse profile can be reproduced with either: i) a conventional antipodal polar cap model with a “pencil plus fan” beam intensity pattern; or ii) emission regions on the stellar surface that are significantly elongated in longitude (i.e., in the direction of rotation). Although in the analysis presented above only approximations to emission models were considered for the sake of computational efficiency, the main findings are likely to remain valid for a more realistic treatment employing sophisticated atmosphere models of various surface magnetic field strengths and chemical compositions.

Given that the observed thermal X-ray radiation from CCOs is due to passive cooling, the inferred temperature distribution suggests highly anisotropic heat conduction from the stellar interior. As posited by several existing studies (Halpern & Gotthelf 2010; Ho 2011; Viganò & Pons 2012; Shabaltas & Lai 2012; Bernal et al. 2013; Perna et al. 2013; Gotthelf et al. 2013) if the heated regions on the surface of PSR J1852+0040 are closely associated with the magnetic field structure, strong magnetic fields beneath the stellar surface are required to channel heat to a relatively small portion of the star. The constraints on the heat distribution of PSR J1852+0040 presented herein further support the argument that rather than being born with intrinsically weak fields, CCOs possess strong “hidden” magnetic fields that were buried due to rapid accretion of fallback material shortly after the supernova explosion. This burial hypothesis avoids the requirement for a strong external global dipole magnetic field, which would manifest in the spin-down measurement.

An offset dipole can provide a plausible explanation for the two surface temperature maps deduced in §3 for PSR J1852+0040, while still being consistent with the weak field inferred from the pulsar spin-down. In particular, for the “pencil plus fan” beaming model, the implied strong surface field ( $\gtrsim 10^{12}$  G) needed to produce such a highly anisotropic emission pattern can be explained by a magnetic moment that is significantly displaced mostly along the axial direction of the dipole (Figure 7a). This configuration can also account for the two hot spots that differ greatly in size and temperature for the CCO in Puppis A, PSR J0821–4300. The linear geometry of the heated regions required for the isotropic and cosine beaming patterns can be produced if the offset of the dipole is in a direction orthogonal to the magnetic axis (Figure 7b). The large field displacements in both cases are possibly a consequence of an off-center supernova explosion.

A phase-resolved spectroscopic analysis reveals no phase-dependent narrow-band features that could arise due to cyclotron absorption/scattering. In addition, although the same single-temperature C atmosphere model applied to the CCOs in Cas A and G353.6–0.7 produces a satisfactory fit to the spectrum of PSR J1852+0040, the implied emitting area at pulse maximum is compa-

rable to the total neutron star surface area. This finding is difficult to reconcile with the observed large amplitude X-ray pulsations, suggesting that similar results obtained for other CCOs, especially G353.6–0.7, may not be valid as well.

In future investigations, it is important to employ realistic atmospheres in modeling the X-ray emission from PSR J1852+0040. As noted previously, since the exact magnetic field and chemical composition for CCOs, in general, are quite uncertain, a wide variety of models need to be considered. Moreover, substantially deeper X-ray observations are needed to better constrain the energy-dependence and reveal the small-scale details of the pulse profile, especially in the pulse peak and trough, to further constrain the details of the surface heat distribution and, by extension, the magnetic field topology. In the theoretical realm, it is crucial to investigate the surface heat signatures of non-standard magnetic field configurations (e.g., non-star-centered and

non-axisymmetric), since they appear to be required to reproduce the phenomenology of PSR J1852+0040.

I thank E. V. Gotthelf for helpful tips regarding the data reduction, J. P. Halpern for insightful discussions, and the anonymous referee whose helpful comments resulted in substantial improvements in the manuscript. This project was supported by NASA Astrophysics Data Analysis Program (ADAP) grant NNX12AE24G. The work presented was based on observations obtained with *XMM-Newton*, an ESA science mission with instruments and contributions directly funded by ESA Member States and NASA. This research has made use of the NASA Astrophysics Data System (ADS) and data obtained from the High Energy Astrophysics Science Archive Research Center (HEASARC), provided by NASA's Goddard Space Flight Center.

Facilities: *XMM-Newton* (EPIC)

## REFERENCES

- Arnaud, K. A. 1996, *ASPC*, 101, 17
- Beloborodov, A. M. 2002, *ApJ*, 566, 85
- Bernal, C. G., Page, D., & Lee, W. H. 2013, *ApJ*, 770, 106
- Bignami, G. F., Caraveo, P. A., De Luca, A., Mereghetti, S. 2003, *Nature*, 423, 725
- Blondin, J. M. 1986, *ApJ*, 308, 755
- Bogdanov, S., & Grindlay, J. E. 2009, *ApJ*, 703, 1557
- Burrows, A., & Hayes, J. 1996, *PhRvL*, 76, 352
- Chang, P., & Bildsten, L. 2004, *ApJ*, 605, 830
- Chang, P., Bildsten, L., Arras, P. 2010, *ApJ*, 723, 719
- Chevalier, R. A. 1989, *ApJ*, 346, 847
- Cropper, M., Zane, S., Ramsay, G., Haberl, F., & Motch, C. 2001, *A&A*, 365, 302
- De Luca, A., Mereghetti, S., Caraveo, P. A., Moroni, M., Mignani, R. P., & Bignami, G. F. 2004, *A&A*, 418, 625
- de Luca, A. 2008, *AICP*, 983, 311
- Fesen, R. A., Hammell, M. C., Morse, J., Chevalier, R. A., Borkowski, K. J., Dopita, M. A., Gerardy, C. L., Lawrence, S. S., Raymond, J. C., van den Bergh, S. 2006, *ApJ*, 645, 283
- Ftaclas, C., Kearney, M. W., & Pechenick, K. 1986, *ApJ*, 300, 203
- Geppert, U., Page, D., & Zannias, T. 1999 *A&A*, 345, 847
- Geppert, U., Küker, M., Page, D. 2006, *A&A*, 457, 937
- Giacani, E., Smith, M. J. S., Dubner, G., Loiseau, N., Castelletti, G., & Paron, S. 2009, *A&A*, 507, 841
- Gotthelf, E. V., et al. 2005, *ApJ*, 627, 390
- Gotthelf, E. V., & Halpern, J. P. 2009, *ApJ*, 695, 35
- Gotthelf, E. V., Perna, R., & Halpern, J. P. 2010, *ApJ*, 724, 1316
- Gotthelf, E. V., Halpern, J. P., & Alford, J. 2013, *ApJ*, 765, 58
- Hailey, C. J., & Mori, K. 2002, *ApJ*, 578, 133
- Halpern, J. P., & Gotthelf, E. V. 2010, *ApJ*, 709, 436
- Heyl, J. S., & Hernquist, L. 1998, *MNRAS*, 300, 599
- Heyl, J. S., & Hernquist, L. 2001, *MNRAS*, 324, 292
- Ho, W. C. G., & Heinke, C. O. 2009, *Nature*, 462, 71
- Ho, W. C. G., & Lai, D. 2001, *MNRAS*, 327, 1081
- Ho, W. C. G., Potekhin, A. Y., & Chabrier, G. 2008, *ApJS*, 178, 102
- Ho, W. C. G. 2011, *MNRAS*, 414, 2567
- Ho, W. C. G. 2013, *IAUS*, 291, 101
- Houck, J. C., & Chevalier, R. A. 1991, *ApJ*, 376, 234
- Kargaltsev, O., Durant, M., Misanovic, Z., Pavlov, G. G. 2012, *Science*, 337, 946
- Kaspi, V. M. 2010, *PNAS*, 107, 16
- Klochkov, D., Pühlhofer, G., Suleimanov, V., Simon, S., Werner, K., Santangelo, A. 2013, *A&A*, 556, 41
- Lai, D., & Goldreich, P. 2000, *ApJ*, 535, 402
- McClintock, J. E., Narayan, R., & Rybicki, G. B. 2004, *ApJ*, 615, 402
- Miller, M. C. & Lamb, F. K. 1998, *ApJ*, 499, L37
- Mori, K., Chonko, J. C., Hailey, C. J. 2005, *ApJ*, 631, 1082
- Mori, K., & Ho, W. C. G. 2007, *MNRAS*, 377, 905
- Muslimov, A. & Page, D. 1995, *ApJ*, 440, L77
- Pavlof, G. G., & Lune, G. J. M. 2009, *ApJ*, 703, 910
- Pavlov, G. G., Shibano, Yu. A., J. Ventura, J., & Zavlin, V. E. 1994, *A&A*, 289, 837
- Pechenick, K. R., Ftaclas, C., & Cohen, J. M. 1983, *ApJ*, 274, 846
- Pérez-Azorín, J. F., Miralles, J. A., Pons, J. A. 2006, *A&A*, 451, 1009
- Perna, R., Viganó, D., Pons, J. A., & Rea, N. 2013, *MNRAS*, 434, 2362
- Pons, J. A., Miralles, J. A., Geppert, U. 2009, *A&A*, 496, 207
- Posselt, B., Pavlov, G. G., Suleimanov, V., Kargaltsev, O. 2013, *ApJ*, 779, 186
- Possenti, A., Cerutti, R., Colpi, M., Mereghetti, S. 2002, *A&A*, 387, 993
- Potekhin, A. Y., & Yakovlev, D. G. 2001, *A&A*, 374, 213
- Potekhin, A. Y., Suleimanov, V. F., van Adelsberg, M., Werner, K. 2012, *A&A*, 546, 121
- Poutanen, J. & Gierliński, M. 2003, *MNRAS*, 343, 1301
- Psaltis, D., Özel, F., & DeDeo, S. 2000, *ApJ*, 544, 390
- Rajagopal, M. & Romani, R. W. 1996, *ApJ*, 461, 327
- Riffert, H. & Mészáros, P. 1988, *ApJ*, 325, 207
- Romani, R. W. 1987, *ApJ*, 313, 718
- Sanwal, D., Pavlov, G. G., Zavlin, V. E., Teter, M. A. 2002, *ApJ*, 574, L61
- Seward, F., Slane, P., Smith, R., Sun, M. 2002, *APRN*17035S
- Shabaltas, N., & Lai, D. 2012, *ApJ*, 748, 148
- Shibanov, Yu. A., Zavlin, V. E., Pavlov, G. G., & Ventura, J. 1992, *A&A*, 266, 313
- Spitkovsky, A. 2006, *ApJ*, 648, L51
- Strüder, L. et al. 2001, *A&A*, 365, L18
- Suleimanov, V. F., Pavlov, G. G., & Werner, K. 2010, *ApJ*, 714, 630
- Suleimanov, V. F., Pavlov, G. G., Werner, K. 2012, *ApJ*, 751, 15
- Suleimanov, V. F., Klochkov, D., Pavlov, G. G., Werner, K. 2014, *ApJS*, 210, 13
- Sun, M., Seward, F. D., Smith, R. K., Slane, P. O. 2004, *ApJ*, 605, 742
- Tian, W. W., Leahy, D. A., Haverkorn, M., Jiang, B. 2008, *ApJ*, 679, L85
- Turolla, R., & Nobili, L. 2013, *ApJ*, 768, 147
- van Adelsberg, M., & Lai, D. 2006, *MNRAS*, 373, 1495
- Viganó, D., & Pons, J. A. 2012, *MNRAS*, 425, 2487
- Viganó, D., Rea, N., Pons, J. A., Perna, R., Aguilera, D. N., Miralles, J. A. 2013, *MNRAS*, 434, 123
- Viironen, K. & Poutanen, J. 2004, *A&A*, 426, 985
- Weinberg, N., Miller, M. C., & Lamb, D. Q., 2001, *ApJ*, 546, 1098
- Woltjer, L. 1964, *ApJ*, 140, 1309
- Yakovlev, D. G. & Pethick, C. J. “Neutron Star Cooling” 2004, *ARA&A*, 42, 169
- Zavlin, V. E., Pavlov, G. G., Shibanov, Yu. A., Ventura, J. 1995, *A&A*, 297, 441
- Zavlin, V. E., Pavlov, G. G., Shibanov, Yu. A. 1996, *A&A*, 315, 141